

UNIVERSITÀ DEGLI STUDI DI MILANO

Facoltà di Scienze e Tecnologie Laurea Triennale in Fisica

Accurate relaxation of a 2D crystal interacting with a quasicrystalline potential

Advisor: Prof. Nicola Manini

Mario Forzanini Matricola n° 942222 A.A. 2022/2023

Codice PACS: 61.44.Br

Accurate relaxation of a 2D crystal interacting with a quasicrystalline potential

Mario Forzanini Dipartimento di Fisica, Università degli Studi di Milano, Via Celoria 16, 20133 Milano, Italia

October 25, 2023

Abstract

We investigate the total energy of a hexagonal 2D elastic monolayer interacting with a rigid decagonal quasicrystalline corrugation potential, as a function of their mutual alignment angle. We compare the effectiveness and applicability of several standard numeric optimization techniques, addressing specifically the issue of identifying the optimal angular orientation. We compare our numerical findings with an extension of the Novaco-McTague theory of epitaxial alignment.

Advisor: Prof. Nicola Manini

Contents

1	Intr	oduction	3		
	1.1	The Frenkel-Kontorova model	3		
	1.2	The Novaco-McTague theory	4		
2	The	model	6		
3	Tec	nnical implementation	8		
	3.1	Steepest descent	9		
	3.2	Conjugate gradient	9		
	3.3	Quickmin	9		
	3.4	FIRE	10		
	3.5	Simulated annealing	10		
	3.6	Numerical protocol	11		
4	Results				
	4.1	Finite-size effects	12		
	4.2	Small corrugation range	13		
	4.3	Comparison of minimization methods	14		
	4.4	Simulated annealing	14		
	4.5	The Novaco-McTague angle and distortion pattern	15		
5	Disc	cussion and Conclusion	19		
A	Pro	blems found in previous works	20		

1 Introduction

1.1 The Frenkel-Kontorova model

One of the models apt to describe nanofriction is the Frenkel-Kontorova model which, in its simplest formulation, consists of a 1D chain of atoms, interacting with a fixed sinusoidal potential. The Hamiltonian of the interacting system is:

$$H = \sum_{i=1}^{N} \left[rac{\mathbf{p}_{i}^{2}}{2M} + rac{K}{2} (x_{i+1} - x_{i} - a_{\mathrm{coll}})^{2} + V_{0} \left(1 - \cos \left(rac{2\pi}{a_{\mathrm{pot}}} x_{i}
ight)
ight) \right], \qquad (1)$$

where $a_{\rm coll}$ is the rest length of the adsorbate bonds, and $a_{\rm pot}$ is the characteristic length scale of the substrate potential. The properties of the system depend on the competition of these two length scales expressed by the mismatch ratio $\rho = a_{\rm pot}/a_{\rm coll}$ that can be visualized as the number of atoms per potential well. Now if ρ is any integer, a lattice-matched state, the friction is maximum as moving the chain requires climbing all of the potential wells simultaneously. Adding or removing particles to a lattice-matched state causes topological excitations such as kinks, antikinks or solitons. As long as ρ is a rational number, pinning and therefore a nonzero static friction is predicted.

If ρ is irrational instead, which can only occur in the $N \to \infty$ limit, the resulting incommensurate configurations exhibit a rich phenomenology and are characterized by non-periodic spatially modulated structures. For incommensurate systems the crucial parameter is the dimensionless coupling parameter:

$$g = \frac{V_0}{Ka_{\text{coll}}^2}. (2)$$

Intuitively speaking, when $g\gg 1$ it is very costly for any particle to move across potential wells, while it is comparatively cheaper (energy-wise) to locally deform the chain with the chain particles moving very close to the sinusoidal-potential minima. In such condition it takes a large force to unpin the chain and set it into motion: for this reason such states are pinned, like in the commensurate case. On the other hand, when $g\ll 1$ the set of ground state configurations is continuous, such states are referred to as sliding because the chain can be set into motion by any arbitrarily small driving force, a condition of vanishing static friction called superlubricity[1].

The Frenkel-Kontorova model is a useful tool to understand several key problems in the physics of friction and in other fields of research, but its 1D nature renders it inadequate to describe surface-surface interactions. 2D problems indeed add a new degree of freedom to the system, as the ground state energy generally comes to depend on the relative orientation of the adsorbed and surface layers.

1.2 The Novaco-McTague theory

Following the Novaco-McTague approach [2, 3], we consider a harmonic crystalline monolayer, with Hamiltonian:

$$H_0 = \sum_{j} \frac{\hat{\mathbf{p}}^2}{2M} + \frac{1}{2} \sum_{j,j'} \phi_{jj'}^{\alpha\alpha'} u_{j\alpha} u_{j'\alpha'},$$
 (3)

where $\mathbf{u}_j = \mathbf{r}_j - \mathbf{R}_j$ is the displacement from the lattice equilibrium position \mathbf{R}_j and ϕ is the Hessian matrix of the interaction. For simplicity, following Novaco-McTague [2, 3], we assume that the atomic displacements are restricted to the "horizontal" 2D x-y plane, while "vertical" z displacements are prohibited. The adsorbed layer then interacts with a fixed surface potential:

$$\hat{V}(\mathbf{r}) = -V_0 \left| \sum_{j=1}^{N_s} \frac{e^{i\mathbf{k}_j \cdot \mathbf{r}}}{N_s} \right|^2 = -\frac{V_0}{N_s^2} \left(\sum_{\mathbf{G}} e^{-i\mathbf{G} \cdot \mathbf{r}} + N_s \right),$$
 (4)

where V_0 is the potential amplitude, a_{pot} is the characteristic length scale of the potential, k denotes a reciprocal vector generating the potential, pointing to the vertices of a regular polygon:

$$\mathbf{k}_{m} = \frac{2\pi}{a_{pot}} \left(\cos \left(\frac{2\pi(m-1)}{N_{s}} \right), \sin \left(\frac{2\pi(m-1)}{N_{s}} \right) \right)^{T}, \tag{5}$$

and G are the vectors connecting the $N_s(N_s-1)$ pairs of k:

$$\forall m, m' \in 1, ..., N_s : m \neq m', G = k_m - k_{m'}.$$
 (6)

Removing the constant additive term in Eq. (4), we are left with a zero-average potential:

$$V(\mathbf{r}) = -\frac{V_0}{N_s^2} \sum_{\mathbf{G}} e^{-i\mathbf{G} \cdot \mathbf{r}} = -\frac{V_0}{N_s^2} \sum_{\mathbf{G}} \cos(\mathbf{G} \cdot \mathbf{r}). \tag{7}$$

In the last passage we take advantage of the fact that, in the summation, every G has an opposite partner -G, leading to the cancellation of the imaginary parts. In summary, the Hamiltonian of the interacting system is:

$$H = H_0 + \sum_{j} V(\mathbf{r}_j). \tag{8}$$

For small displacements, $e^{-i\mathbf{G}\cdot\hat{\mathbf{u}}_j}\approx 1-i\mathbf{G}\cdot\hat{\mathbf{u}}_j$. If in H_0 we neglect the kinetic term (and therefore all quantum effects), the ground state of the system is

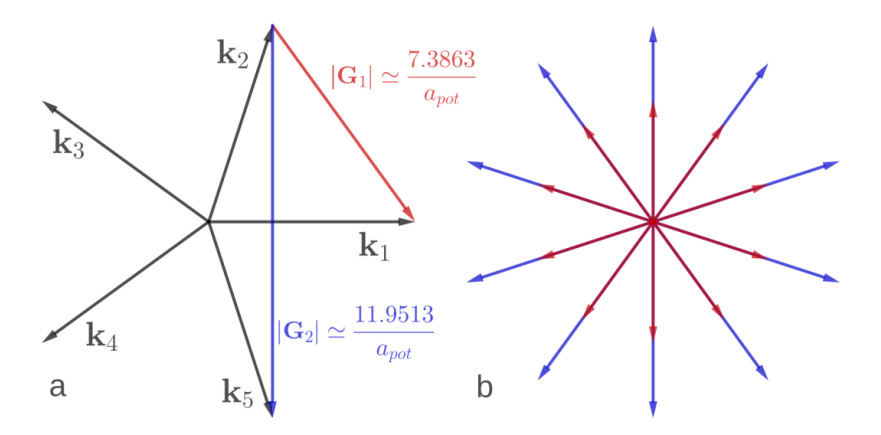


Figure 1: a) The k vectors of the potential's reciprocal lattice and the geometric construction to obtain the G vectors.
b) A sketch of the 20 G vectors.

obtained by minimizing the total potential energy. The result valid in the limit of weak coupling $(V_0 \to 0)$ is the following:

$$\begin{cases} \epsilon_{1\text{-ph}} = -\frac{V_0^2}{2MN_s^4} \sum_{q}^{BZ \setminus O} \sum_{s=L,T} \frac{\left| f_{q,s} \right|^2}{\omega_{q,s}^2} \\ f_{q,s} = \sum_{\mathbf{G}} \sum_{\tau} \mathbf{G} \cdot \epsilon_{q,s} e^{-i\tau \cdot \mathbf{R}_0} \delta_{q,\mathbf{G}-\tau}, \end{cases}$$
(9)

where \mathbf{R}_0 is the origin of the adatom lattice, τ denote crystal reciprocal lattice vectors, $\epsilon_{\mathbf{q},s}$ and $\omega_{\mathbf{q},s}$ are the phonon polarization vectors and phonon frequencies. Here s=L,T labels the longitudinal and transverse modes, obtained by the usual diagonalization of the Fourier-transformed dynamical matrix:

$$D(\mathbf{q})\epsilon_{\mathbf{q},s} = \omega_{\mathbf{q},s}^2 \epsilon_{\mathbf{q},s}. \tag{10}$$

The original Novaco-McTague theory considers a crystalline potential, such as the one obtained for $N_s=3$ or 4. However this theory is generalized in a straightforward fashion for the quasiperiodic case by taking $N_s=5$. In this condition, the generating polygon is a regular pentagon, and the G vectors containing the Fourier components of the potential form 2 concentric regular decagons, as illustrated in Figure 1.

Our work seeks to validate these results in the case of a harmonic triangular lattice interacting with a pentagonal quasicrystalline surface. This is a step towards validating the results obtained in several studies of the frictional properties of this system[4, 5, 6, 7], all of which depend on the accurate individuation of the static ground state.

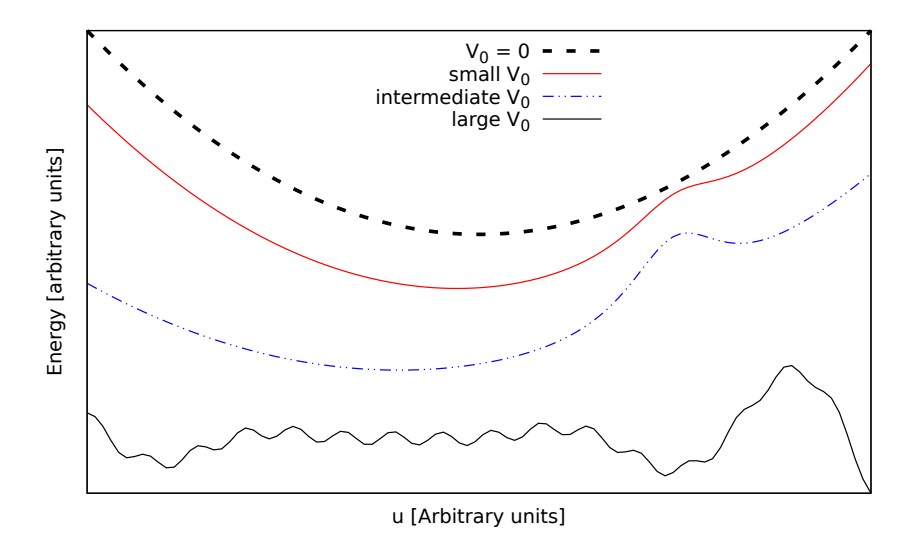


Figure 2: A 1-dimensional sketch of the total potential as a function of a fictitious displacement coordinate, for 4 different and increasing values of the amplitude V_0 of the quasicrystalline substrate corrugation. When the corrugation contribution remains within the perturbative range there still is one single global minimum, adiabatically connected to the unperturbed one at u=0. As the corrugation amplitude V_0 further increases, the landscape starts to exhibit local minima and eventually the global minimum loses any connection to the unperturbed state.

2 The model

Our model consists of a 2D colloidal monolayer interacting with a decagonal quasi-periodic substrate. The Hamiltonian of the system is given by Eq. (3). Let us denote the colloidal-colloidal interaction with U_{cc} . Even though a realistic interaction between colloids is usually modeled by a highly anharmonic potential such as the Yukawa one [8], to avoid anharmonic effects in comparing with Novaco-McTague's theory we consider it to be harmonic:

$$U_{cc} = \frac{K}{2} \sum_{i,j} \left(\left| \mathbf{r}_i - \mathbf{r}_j \right| - a_{\text{coll}} \right)^2, \tag{11}$$

where the spring constant $K = 0.2 \text{zJ} \mu\text{m}^{-2}$ is coherent with previous works where the particles where considered as point-charges interacting through a (highly anharmonic) screened Coulomb potential[9, 10].

For $V_0 = 0$ we expect the only stationary point of the total energy of the system to be the absolute minimum of the colloid-colloid harmonic potential,

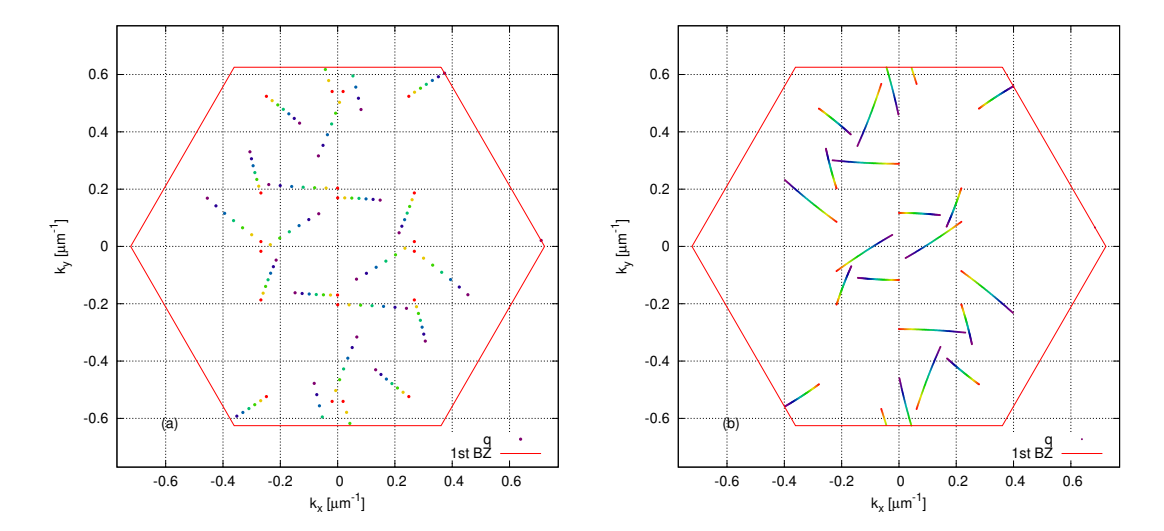


Figure 3: Red hexagon: first Brillouin zone of the triangular lattice, for $a_{\rm coll}=5.8\,\mu{\rm m}$. Dots: successive locations of the **q** points obtained by Eq. (12), as the **G** vectors of the quasicrystalline potential are rotated from 0° (red) to 6° (purple) counterclockwise. Each of the 20 **G** points generates one of these **q** points through Eq. (12). Panel (a): $a_{\rm pot}=5.2\,\mu{\rm m}$, highly mismatched; Panel (b): $a_{\rm pot}=5.4\,\mu{\rm m}$, less mismatched at the optimal angle.

i.e. the perfect crystalline state. As V_0 increases, the competition between U_{cc} and V can give rise to other local minima. However, as long as the amplitude V_0 remains within a small range where the quasiperiodic potential can be considered a weak perturbation to a very rigid crystal, the minimum is still unique and adiabatically connected to the perfect crystal configuration. See Figure 2 for a sketch of this situation. This weak-coupling regime is the one that is described by the Novaco-McTague theory.

The natural energy scale for this system is $Ka_{\rm coll}^2$. For the adopted value $a_{\rm coll}=5.8\,\mu{\rm m}$ and $K=0.2\,{\rm zJ}$, the energy scale is $Ka_{\rm coll}^2=6.728\,{\rm zJ}$. In the present 2D model the dimensionless coupling parameter, analogous to the Frenkel-Kontorova g parameter, is $V_0/(Ka_{\rm coll}^2)$.

The decagonal symmetry of the potential, coupled with the symmetries of the triangular lattice, reduces the angular range to study to 12°, which can be further reduced to $0^{\circ}-6^{\circ}$ by noting the angular inversion symmetry $\theta \rightarrow -\theta$ in the potential.

To apply the extended Novaco-McTague's theory Eq. (9) we are interested in the difference between its G vectors Eq. (6) and the vectors of the colloidal reciprocal lattice, τ . Due to the delta condition in Eq. (9) we identify

$$\mathbf{q} = \mathbf{G} - \tau. \tag{12}$$

We propose to study the incommensurate case, so the two length scales a_{pot} and a_{coll} have to be such that $\forall \mathbf{G}, \tau, \theta : \mathbf{q} \neq \mathbf{0}$. Here θ is the mutual-orientation angle by which the corrugation potential (and thus the \mathbf{G} vectors) is rotated relative to the crystalline principal directions of the colloidal lattice. For the adopted value $a_{pot} = 5.2 \, \mu \text{m}$, Figure 3a shows that, for any mutual-orientation angle, \mathbf{q} remains well clear from $\mathbf{0}$. The alternative choice $a_{pot} = 5.4 \, \mu \text{m}$, Figure 3b, shows that, at the optimal angle, \mathbf{q} comes substantially closer to $\mathbf{0}$: this is still an incommensurate geometry, which comes nearer to commensurate.

3 Technical implementation

In this chapter we present the technical implementation of the simulations of the physical system described in Sect. 2. We cut a circular sample out of a large portion of a triangular lattice with spacing $a_{\rm coll}$. To mantain a good control of the angular orientation of the adsorbate layer and to avoid unwanted twists or scale deformations, we choose to rigidly set the positions of the atoms at the edge of the sample to perfect-lattice positions. The total potential energy is therefore a function of the x and y coordinates defining the positions (or, equivalently, the displacements) of all colloids inside this rigid ring. Our task is to minimize this function, for different values of the mutual angular orientation θ , fixed by the external rigid ring.

The problem of finding the global minimum of a complicated multidimensional function is recurring in many fields of science and several methods have been developed to solve it; some of these algorithms rely on molecular dynamics to explore the potential landscape, while others are inspired by real-world processes that lead to the formation of large scale ordered structures. Our simulations make use of LAMMPS' [11] implementation of several well-known minimization algorithms which will be discussed in detail in the following subsections. Each of these algorithms is formulated in such a way that it terminates when the difference in energy between two consecutive steps or the absolute value of the force becomes lower than two respective thresholds defined by the user. In our simulations we decided to only set force thresholds, that we fixed as a small fraction of the typical force $V_0/a_{\rm pot}$, associated to the corrugation amplitude V_0 .

To avoid incurring in local minima different from the global ground state, we apply multiple minimization techniques, including those capable of overcom-

ing the barriers between minima. We also compare and discuss the effectiveness and applicability of the various methods to the problem at hand.

3.1 Steepest descent

Steepest descent is probably the simplest method for minimization in multiple dimensions. It consists of a sequence of line minimizations along the direction of the local downhill gradient.

3.2 Conjugate gradient

The conjugate gradient method is different from steepest descent insofar as it computes new minimization directions so that they are conjugate to the old gradient[12].

Let $f: \mathbb{R}^N \to \mathbb{R}$ be the function to be optimized, let $\mathbf{P} \in \mathbb{R}^N$ be a particular point chosen as the origin of the coordinate system, then f can be approximated by its Taylor series:

$$f(\mathbf{x}) = f(\mathbf{P}) + \sum_{i=1}^{N} \frac{\partial f}{\partial x^{i}} x^{i} + \frac{1}{2} \sum_{i=1}^{N} \sum_{j=1}^{N} \frac{\partial^{2} f}{\partial x^{i} \partial x^{j}} x^{i} x^{j} + \dots = c - \mathbf{b} \cdot \mathbf{x} + \frac{1}{2} \mathbf{x} \cdot \mathbf{A} \cdot \mathbf{x} + o(\|\mathbf{x}\|^{3}),$$
(13)

where

$$c := f(\mathbf{P}), \quad \mathbf{b} := -\nabla f \Big|_{\mathbf{P}}, \quad A_{ij} := \frac{\partial^2 f}{\partial x^i \partial x^j} \Big|_{\mathbf{P}}.$$
 (14)

By differentiating Eq. (13), the gradient of f at \mathbf{x} is easily calculated as $\nabla f(\mathbf{x}) = \mathbf{A} \cdot \mathbf{x} - \mathbf{b}$. Now consider two directions \mathbf{u} and \mathbf{v} : the condition that a minimization along \mathbf{v} does not spoil a previous minimization along \mathbf{u} is that the gradient has to still be perpendicular to \mathbf{u} after such minimization, i.e. that \mathbf{u} and \mathbf{v} are conjugate:

$$0 = \mathbf{u} \cdot \delta(\nabla f) = \mathbf{u} \cdot \mathbf{A} \cdot (\delta \mathbf{x}) = \mathbf{u} \cdot \mathbf{A} \cdot \mathbf{v}. \tag{15}$$

When this relation holds pairwise for all members of a set of vectors, they are said to be a conjugate set. LAMMPS implements the conjugate gradient algorithm attributed to Polak and Ribiere[13]. We note that we realized that this method performs better when setting energy thresholds rather than force thresholds.

3.3 Quickmin

The Quickmin algorithm improves upon the steepest descent method by accelerating the system in the direction of the force. It consists of a damped

dynamics routine, where the damping factor is the projection of the velocity along the force. In LAMMPS this method is coupled with an Euler integrator, as described in [14]: first it projects the velocity in the direction of the force:

$$\mathbf{v}_{j} = \left(\mathbf{v}_{j} \cdot \frac{\mathbf{F}_{j}}{\left|\mathbf{F}_{j}\right|}\right) \frac{\mathbf{F}_{j}}{\left|\mathbf{F}_{j}\right|} \tag{16}$$

then, before taking a step of the integrator, if $\mathbf{v}_j \cdot \mathbf{F}_j < 0$ it sets $\mathbf{v}_j = 0$.

3.4 FIRE

FIRE[15], short for Fast Inertial Relaxation Engine, is a minimization algorithm based on the discrete version of the equation:

$$\dot{\mathbf{v}}(t) = \frac{\mathbf{F}}{M} - \gamma(t)|\mathbf{v}(t)| \left(\frac{\mathbf{v}(t)}{|\mathbf{v}(t)|} - \frac{\mathbf{F}(t)}{|\mathbf{F}(t)|}\right). \tag{17}$$

where $\mathbf{F} = -\nabla U(\mathbf{x})$, M is the mass of the atom considered, $\mathbf{v} = \dot{\mathbf{x}}$ is its velocity, U is the potential. The last term in the right-hand side of Eq. (17) allows one to introduce an acceleration in a direction which is steeper than the current direction of motion, when the power $P(t) = \mathbf{F}(t) \cdot \mathbf{v}(t)$ is negative the velocity is reset to 0, the velocity is further mixed with the force vectors according to the following equation:

$$\mathbf{v} = (1 - \alpha)\mathbf{v} + \alpha \frac{\mathbf{F}}{|\mathbf{F}|}|\mathbf{v}| \tag{18}$$

which results in an Euler discretization of the last term in Eq. (17), where $\alpha = \gamma \Delta t$ and Δt is the integration time step. Both the time step and the mixing coefficient α are dynamically adaptive quantities.

We use LAMMPS' default values for most parameters of the algorithm, except for the time-step which we set to 500 ms because for any longer timestep the minimization would endlessly fluctuate. For a more thorough discussion of the implementation of FIRE in LAMMPS, we refer to Ref. [16].

3.5 Simulated annealing

All algorithms described so far lead from the starting point to the closest (local) minimum, the one sitting inside the same basin of attraction. If a deeper minimum, perhaps the global one, sits further away, none of these methods has any way to discover it. The simulated annealing method is a way around this problem, and a significant step in the quest of a global minimum.

The simulated annealing technique is inspired by the homonymous metallurgical process of heating up a solid and then cooling it slowly until it crystallizes. It is a stochastic method that ensures the convergence of the system to the global minimum, in the limit of infinite cool-down time. After thermalizing the system at an initial temperature T_0 the system is cooled down in steps until $T=0\,\mathrm{K}$. As long as k_BT is of the order of or larger than the energy barrier between minima basins, the exploration has a nonzero probability to transition from the current basin to another basin. Even though at finite temperature the system can hop from the basin of a minimum to that of a less deep one, if the temperature reduction is carried out extremely slowly, one is certain that the minimization will land at the lowest minimum, the true ground state.

The choice of initial temperature is particularly delicate, because it needs to be sufficiently high to promote barrier hopping, but at the same time not too high that it completely disorders the sample, which would make it very costly to cool down to the proper minimum. Assuming that in our problem the barrier height is of the order of V_0 , we adopt an initial temperature T_0 such that $k_BT_0=10\%V_0$.

The results of finite-time simulated annealing procedures could depend on the adopted cooling schedule. We tested the following schedules:

- Geometric schedule: $T_{k+1} = \beta^k T_k$ where $\beta \in [0.8, 0.99]$
- ullet Linear schedule: $T_{k+1} = T_k \Delta T$ where ΔT is a constant decrement
- Exponential schedule: $T_{k+1}=T_ke^{-\beta\frac{k}{N}}$ where $\beta>1$ and N is the total number of linear annealing steps taken

where T_k is the temperature at the k-th step of the cooling schedule. To ensure the complete relaxation of the crystal, after the simulated annealing procedure we run FIRE.

3.6 Numerical protocol

In order to investigate the Novaco effect, we need to be able to compare the $T=0\,\mathrm{K}$ configuration for numerous mutual rotations between the adsorbate layer and the fixed corrugation potential. For practical purposes, rather than keeping the crystal fixed, and rotating the potential by an angle θ , we proceed the other way round, which is perfectly equivalent. We minimize each rotational configuration separately and then collect the relaxed energy differences from each of them in order to compare them to the prediction of Eq. (9). See Table 1 for a summary of the values of parameters used in this work.

Physical quantity	Value
$a_{ m pot}$	5.2μm or 5.4μm
$a_{ m coll}$	5.8 µm
m	31.0593pg
$Ka_{ m coll}^2$	$6.728\mathrm{zJ}$

Table 1: Parameters characterizing our simulations

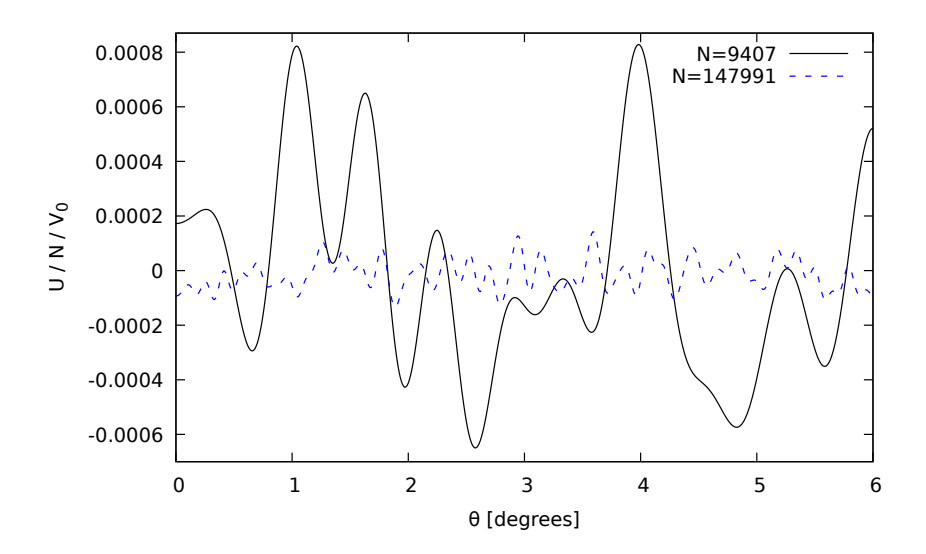


Figure 4: Angular energy fluctuations due to the finite size of the rigid sample. The unrelaxed energy per particle is compared for samples of different size.

4 Results

4.1 Finite-size effects

The Novaco-McTague theory, Sect. 1.2, is developed under the assumption of an infinite adsorbed crystalline layer interacting weakly with an infinitely extended potential. Of course our simulations do not fall within the bounds of these assumptions, so before discussing any results we must quantify the effects of the finite size of our samples on the computed energy.

Due to our choice of zero-average potential, we can predict that the corrugation energy at a randomly placed point vanishes on average. Since the points in the perfect crystal are unrelated to the quasicrystalline potential, they can be seen as random sampling of the latter. Therefore the mean energy per particle of the rigid (unrelaxed) crystal should vanish in the infinite-size limit. As seen in Fig. 4, the fluctuations around the mean energy decrease in amplitude

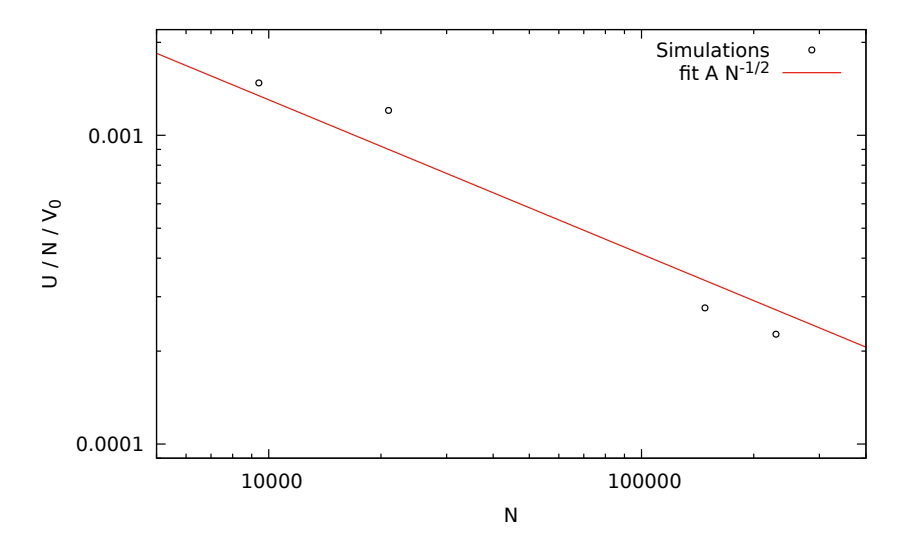


Figure 5: Maximum amplitude of the angular energy fluctuations due to the finite size of the rigid sample, calculated as $\max_{\theta \in [0^{\circ},6^{\circ}]} U - \min_{\theta \in [0^{\circ},6^{\circ}]} U$, for $a_{\text{pot}} = 5.2\,\mu\text{m}$. As expected the energy per particle decreases as $N^{-1/2}$

and increase in frequency as the size of the sample increases. We expect these finite-size effects to be proportional to the number of atoms at the edge of the sample, which in turn is proportional to \sqrt{N} , where N is the total number of particles. Figure 5 indeed shows that the normalized amplitude of the energy fluctuations is compatible with $N^{-1/2}$.

In order to mitigate these finite-size effects, rather than absolute potential energies, we will report differences between the minimized energy and the initial unrelaxed value (namely the energy of the rigid crystal) at the same angle. It makes sense to compare these energy lowerings directly to Eq. (9) because the substrate potential Eq. (7) has zero average value.

4.2 Small corrugation range

Beside finite-size effects, we must determine the values of V_0 for which the corrugation can be considered small when compared to the adsorbed layer's bond energy. In the small corrugation regime we expect a quadratic response in the potential amplitude V_0 , Eq. (9); therefore we evaluate the relaxation energy as a function of the corrugation potential amplitude. Figure 6 shows that corrugations $g = V_0/(Ka_{\text{coll}}^2) < 0.1$ fall well within the weak-coupling range.

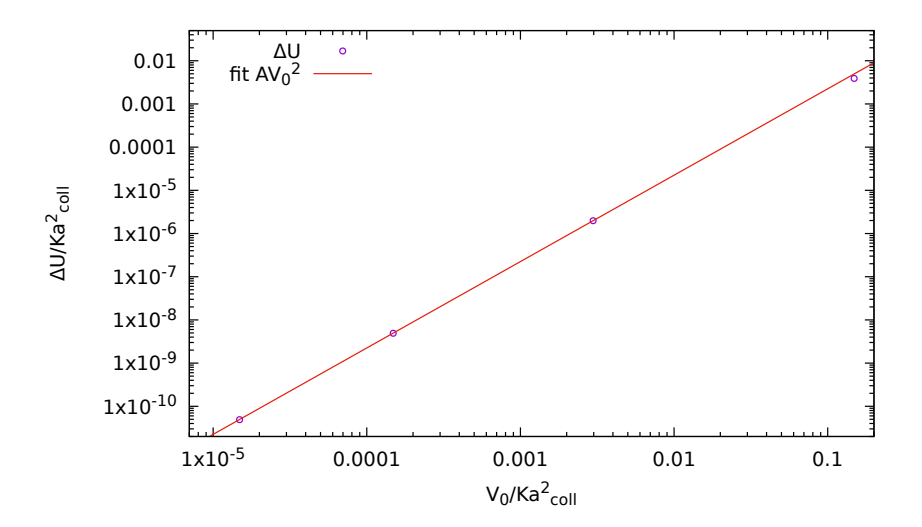


Figure 6: The relaxation energy as a function of the corrugation potential amplitude V_0 , at the optimal misfit angle $\theta=4.2^{\circ}$ for $a_{\rm coll}=5.8\,\mu{\rm m},~a_{\rm pot}=5.2\,\mu{\rm m}.$ The Novaco-McTague theory predicts a quadratic response in V_0 . These results indicate that such quadratic dependence holds for dimensionless coupling strength of the order of 10^{-1} or smaller.

4.3 Comparison of minimization methods

For corrugations exceeding g > 0.1, we cannot be certain that our minimizations do not fall into one of these non-global minima, so we compare the results of different minimization algorithms, or apply them repeatedly to the same sample.

As shown in Figure 7 FIRE and Quickmin lead consistently to identical minima in one single run, while CG turns out to be far slower. After these tests, we adopted the FIRE method as the most efficient one.

4.4 Simulated annealing

After experimenting with deterministic minimization algorithms, we tested different simulated annealing schedules to see if they would yield better results. At the end of simulated annealing procedures we always finalize the relaxation to the nearest local minimum by using FIRE. We used LAMMPS' Langevin thermostat to control the temperature and ramp it down linearly, we then combined multiple linear temperature ramps to emulate more sophisticated cooling schedules.

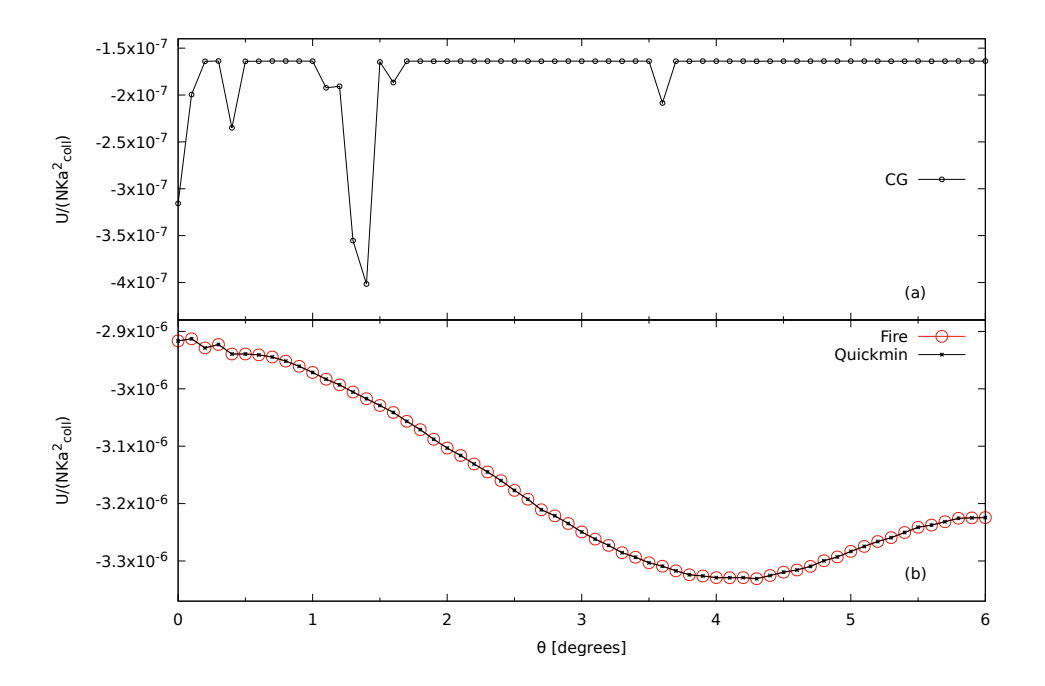


Figure 7: The energy of the relaxed system as a function of the misfit angle θ with $V_0=0.00148Ka_{\rm coll}^2$, $a_{\rm pot}=5.2\,\mu{\rm m}$ and N=147991. Panel (a): CG stops according to an energy threshold of $1\times 10^{-8}\,{\rm zJ}$, or after 100000 minimization steps, clearly not reaching convergence. Panel (b): FIRE and Quickmin stop according to a force threshold of $1\times 10^{-13}\,\mu{\rm N}$, or after a runtime of 50 ms while and clearly lead to the same well-converged energy.

All of the different cooling schedules produce the same result obtained by FIRE minimization, as shown in Figure 8. Furthermore we choose to repeat the linear simulations using different seeds for the Langevin random number generator, in order to further our confidence in the accuracy of the minima found (Figure 9).

4.5 The Novaco-McTague angle and distortion pattern

After testing different minimization methods to identify the most suitable one, we compared the results with the linear-response expression Eq. (9) as a function of the misfit angle. The comparison is shown in Figures 10, 11. The minimizations show a quite good nearly quantitative agreement with the weak-coupling theory. A priori one would expect the numerical minimization results

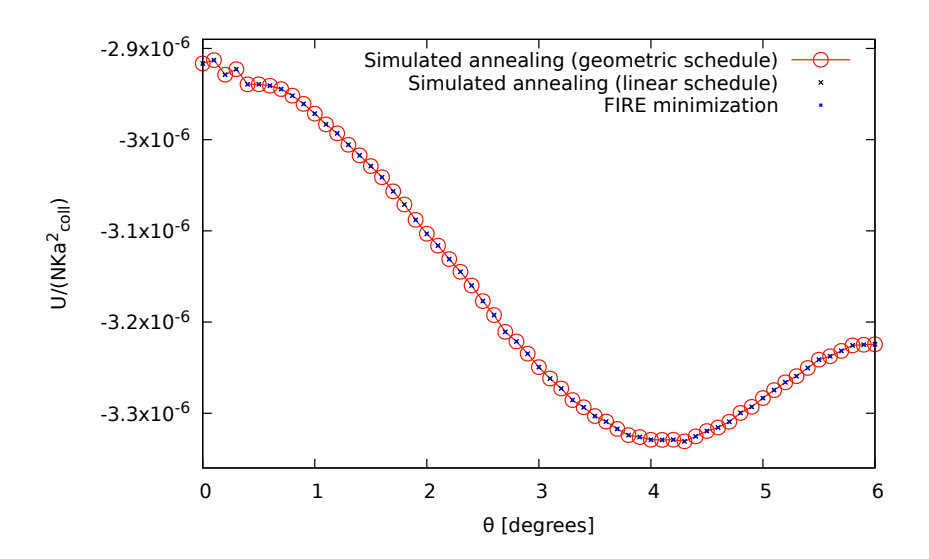


Figure 8: Comparison of the energy of the system as a function of the misfit angle θ after simulated annealing for different cooling schedules. Both linear and geometric cooling schedules give the same results as the FIRE minimization. Parameters for these simulations are the same as in Fig. 7 with $k_BT_0=1.48\times 10^{-4}Ka_{\rm coll}^2=0.1V_0$.

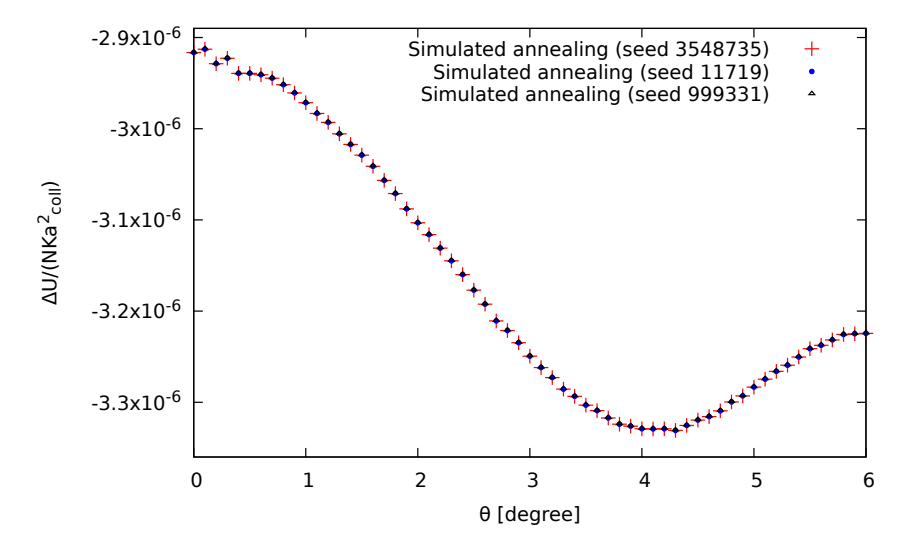


Figure 9: The relaxed energy of the system after simulated annealing as a function of the misfit angle, the figure shows results of the same linear annealing schedule with different seeds for Langevin's random-number generator. The simulation parameters and annealing temperature are the same as in Fig. 8.

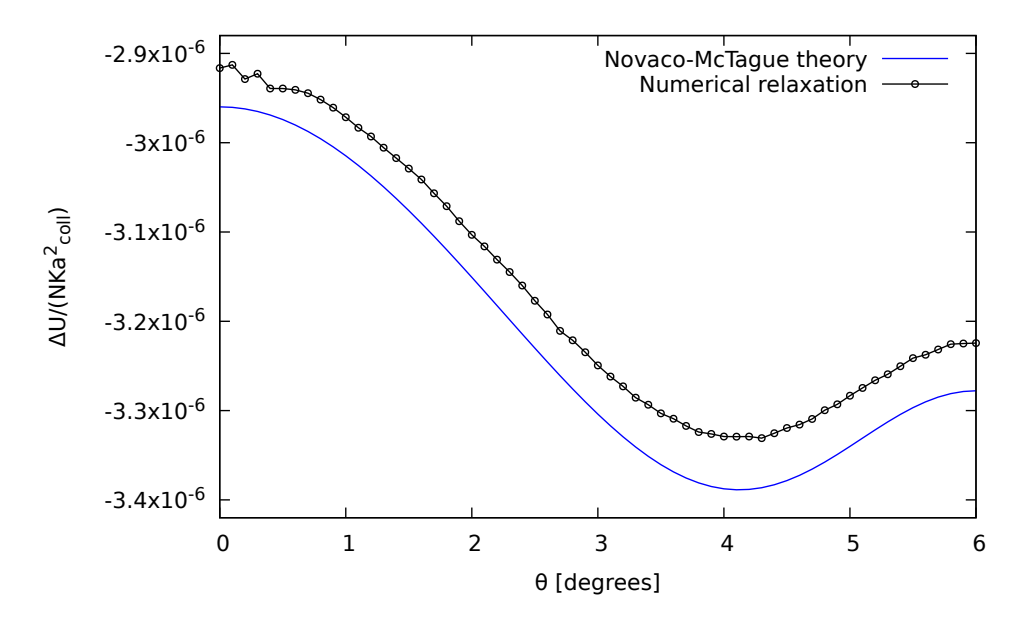


Figure 10: The numerically relaxed total potential energy per particle as a function of the mutual alignment angle θ , compared to the weak-coupling energy profile calculated according to the extended Novaco-McTague theory Eq. (9). The simulation parameters are $V_0 = 0.00148 K a_{\rm coll}^2$, $a_{\rm pot} = 5.2\,\mu{\rm m}$ and N = 147991.

to sit at a lower energy than the approximated one-phonon energy, but the opposite is observed.

The more closely matched the geometry the more prominent we expect the Novaco-McTague minimum to be, given that Eq. (9) depends on the inverse square of the phonon frequencies. We repeated the simulations setting $a_{\rm pot}=5.4\,\mu{\rm m}$, which results in the **q** vectors sketched in Fig. 3b, showing that as theta is varied, at its closest approach **q** comes closer to the origin than for $a_{\rm pot}=5.2\,\mu{\rm m}$ (Fig. 3a). Indeed the resulting angular energy profile shown in Figure 11 exhibits a much deeper minimum than for $a_{\rm pot}=5.2\,\mu{\rm m}$, Fig. 10. The optimal Novaco-McTague angle $\theta_{\rm NM}\simeq 4.12^\circ$ for $a_{\rm pot}=5.2\,\mu{\rm m}$, and $\theta_{\rm NM}\simeq 5.31^\circ$ for $a_{\rm pot}=5.4\,\mu{\rm m}$, evaluated through Eq. (9).

For each angle, the Novaco-McTague theory predicts the precise amount of distortion for each of the 20 phonon modes whose ${\bf q}$ satisfies Eq. (12). The largest distortion will typically be associated to the softer of these phonons, the long-wavelength one associated to the shortest ${\bf q}={\bf q}_{\rm min}$. Figure 12 reports two relaxed configurations at the optimal $\theta_{\rm NM}$. Each particle is colored in a way representing its displacement away from the perfect crystal. The observed

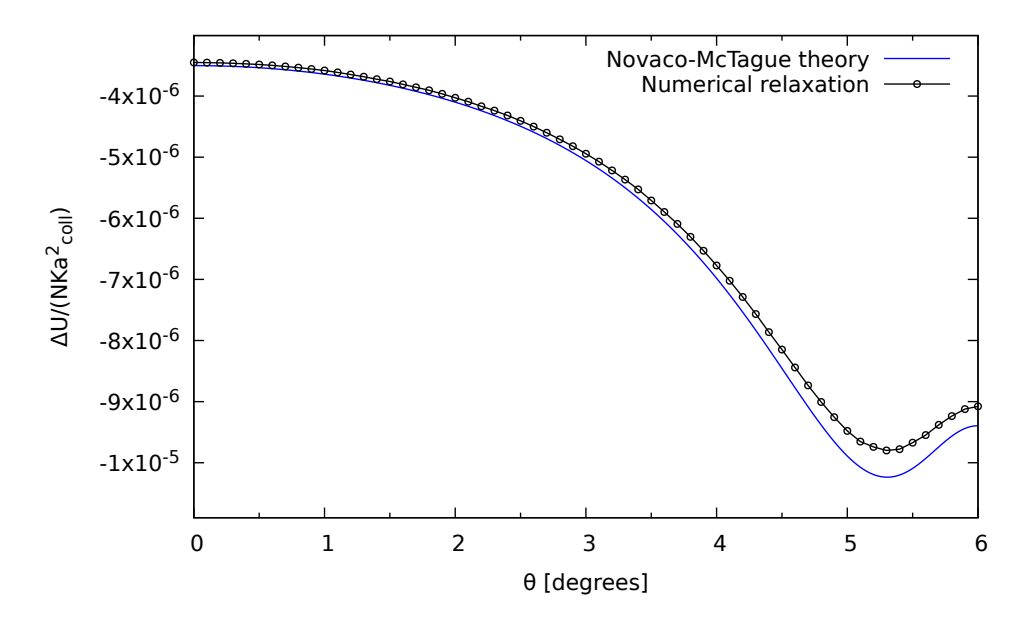


Figure 11: Same as Fig. 10, but for $a_{\rm pot} = 5.4\,\mu\text{m}$, leading to a smaller mismatch at the optimal angle $\theta_{\rm NM} \simeq 5.31^{\circ}$.

displacements are consistent with a dominating phonon wave associated to \mathbf{q}_{\min} , sketched by the corresponding wave fronts. We find a visible agreement between this wave and the observed moirè pattern of displacements.

5 Discussion and Conclusion

In this thesis we solved several practical problems that haunted previous works in this field (see Appendix A). As a main result, we verify quantitatively the extension of the Novaco-McTague theory to the quasicrystalline case for the first time, see Figures 10, 11. We also visualize the distortions associated to the optimal Novaco-McTague angle, proving that they involve significant components of the shortest-q phonons involved.

Small residual differences between the Novaco-McTague weak-coupling formula, Eq. (9), and the results of the numerical minimizations could be due to:

- the fact that the adopted coupling, though relatively small, is finite;
- the finite size of the simulated sample.

Even though verifying these hypotheses would be straightforward, for time constraints we defer these verifications to future work.

The tested minimization methods would allow us to investigate even stronger-coupling regimes with $g \ge 1$, with the need for the search of nontrivial global

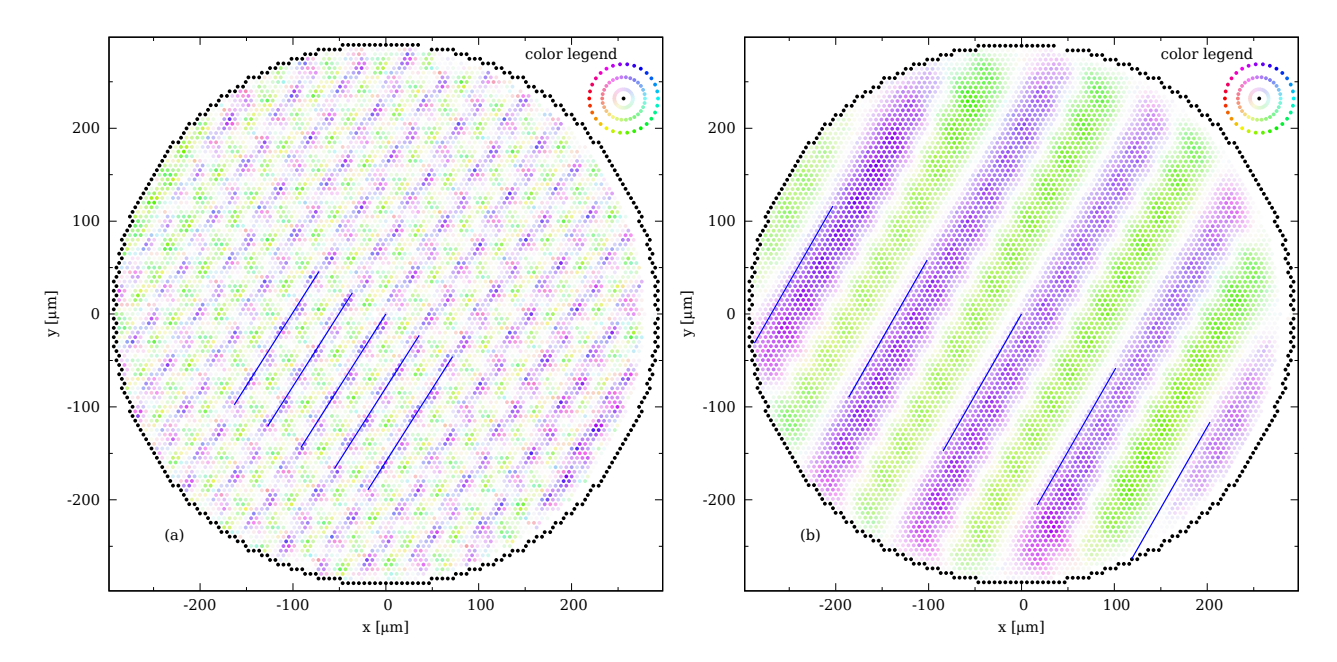


Figure 12: Displacement pattern in the fully-relaxed state at the optimal misfit angle $\theta_{\rm NM}$. The black particles at the edge are the fixed ones, see Sect. 3. The mobile particles in the sample are colored based on their displacement from the perfect crystal configuration: the more intensely colored the particle, the greater its displacement. Blue lines: wavefronts generated by the shortest ${\bf q}$ vector. Panel (a): $a_{\rm pot}=5.2 \, \mu {\rm m}$, $\theta \simeq 4.2^{\circ} \simeq \theta_{\rm NM}$; Panel (b): $a_{\rm coll}=5.4 \, \mu {\rm m}$, $\theta \simeq 5.3 \, \simeq \, \theta_{\rm NM}$.

minima. For the same time constraints, we defer also these investigations to future work.

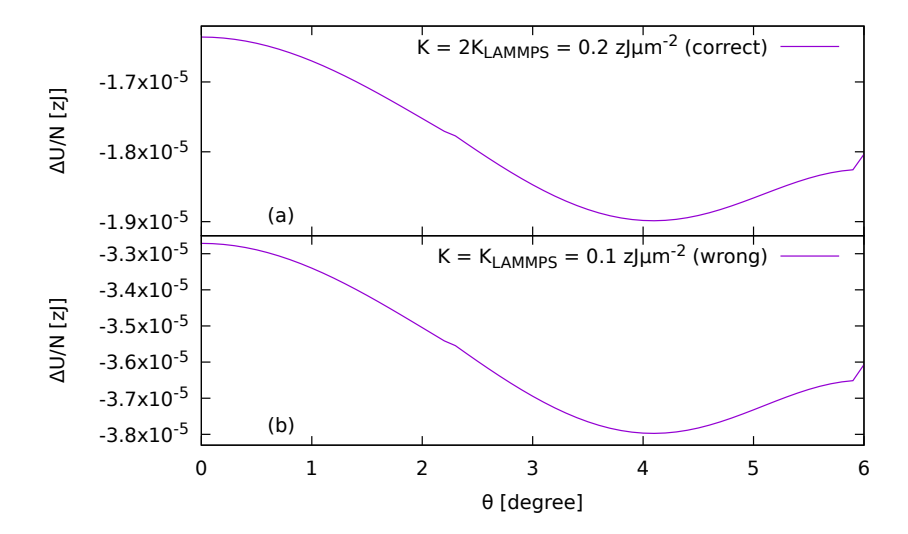


Figure 13: Panel (a): Energy, Eq. (9), as a function of the relative orientation angle θ for $K=2K_{\rm LAMMPS}=0.2\,{\rm zJ\mu m^{-2}}$, which is the correct value. Panel (b): Same as (a) but for $K=K_{\rm LAMMPS}=0.1\,{\rm zJ\mu m^{-2}}$ which does not take into account the nonstandard definition of the spring constant in LAMMPS. All of the other parameters are as in Table 1, with $a_{\rm pot}=5.2\,{\rm \mu m}$.

A Problems found in previous works

The extended Novaco-McTague theory predicts the energy in Eq. (9). Computing this energy numerically presents a number of challenges that we summarize in this appendix. Previous works on this topic [4, 5, 6, 7] reported wrong or excessively approximated calculations that led to quantitative deviations.

First of all we note that previous works that used LAMMPS to perform minimizations failed to notice the nonstandard definitions of the harmonic constant, referred to as K in our work, of LAMMPS differ by a factor of 2:

$$U_{cc} = K_{LAMMPS} \sum_{i,j} \left(\left| \mathbf{r}_i - \mathbf{r}_j \right| - a_{\text{coll}} \right)^2 = [17]$$
 (19)

$$= \frac{K}{2} \sum_{i,j} \left(\left| \mathbf{r}_i - \mathbf{r}_j \right| - a_{\text{coll}} \right)^2. \tag{20}$$

As shown in Figure 13 this error results in qualitatively similar plots but quantitatively different energies.

In Figure 13 one can notice two discontinuous points at $\theta = 2.2^{\circ}$, and $\theta = 6.0^{\circ}$. Zooming in onto these discontinuities (Figure 14) proves that they are not merely an accident dictated by the wide sampling.

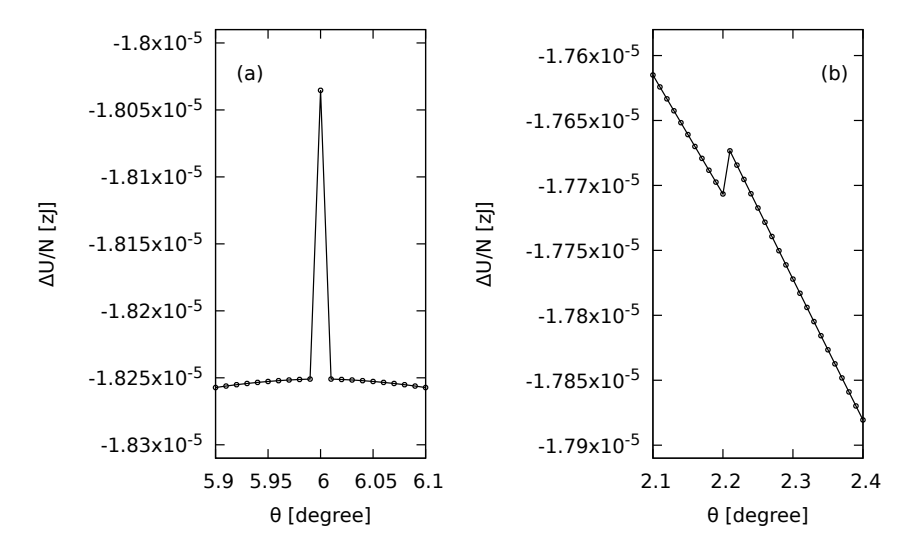


Figure 14: Zoom ins to Fig. 13. Panel (a): artifact discontinuity in the energy profile at $\theta = 6.0^{\circ}$. Panel (b): Artifact discontinuity in the energy profile at $\theta = 2.2^{\circ}$.

The jump at $\theta=6.0^\circ$ is to be attributed to the incorrect identification of the ${\bf q}$ vectors in the first Brillouin zone of the crystal reciprocal lattice. As shown in Figure 3, as the misfit angle changes certain ${\bf q}$ values cross one of the boundaries of the first Brillouin zone, so one needs to be particularly careful to avoid numerical errors when calculating whether or not any of them is inside the first Brillouin zone, any errors in this regard may result in an undercounting, as for $\theta=6.0^\circ$ that affects the energy evaluated according to Eq. (9). We fixed the code that evaluates Eq. (9) in such a way to evaluate correctly the presence of individual ${\bf q}$ vectors in the first Brillouin zone.

Furthermore we acquired the original code for the calculation of Eq. (9), as was used in previous works [4, 5, 6, 7], and it assumed approximate "Debye" phonon polarizations:

$$\epsilon_{\mathbf{q},L} = \frac{\mathbf{q}}{|\mathbf{q}|}, \quad \epsilon_{\mathbf{q},T} = \frac{\left(-q_y, q_x\right)^T}{|\mathbf{q}|},$$
 (21)

and phonon frequencies:

$$\omega_s(\mathbf{q}) = \omega_s(|\mathbf{q}|) = c_s|\mathbf{q}|, \text{ for } s = L, T.$$
 (22)

We decided to improve the code by adopting the exact phonon polarizations

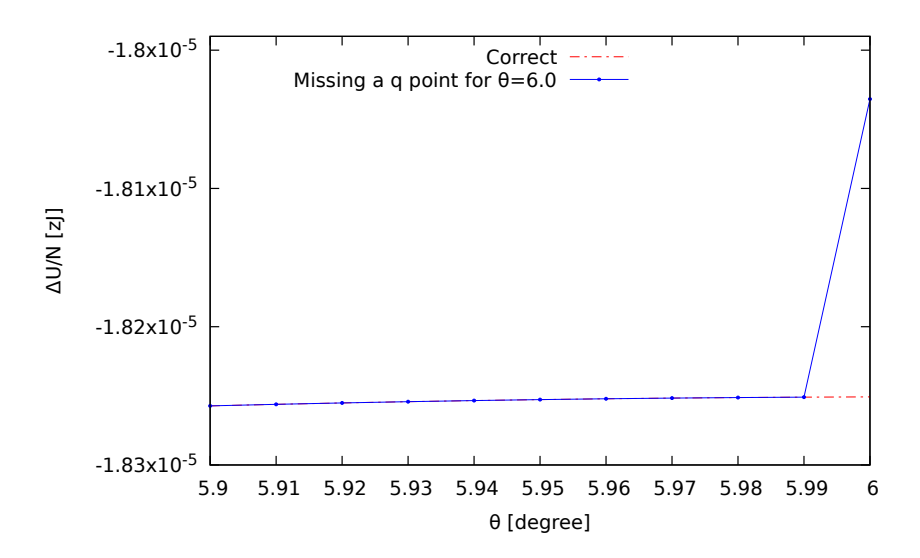


Figure 15: Comparison of the energy profiles obtained after fixing the undercounting problems by properly checking the bounds of the first Brillouin zone. All of the parameters are as in Figure 13.

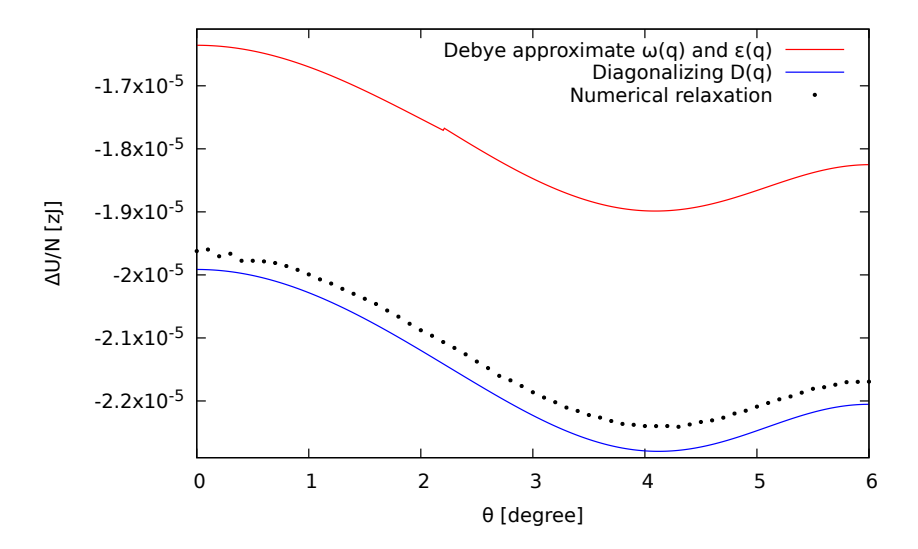


Figure 16: Comparison of the angular energy profile obtained by linearly approximating the phonon frequencies Eq. (22) and polarization vectors Eq. (21) (red) with the one calculated using the exact frequencies and polarization vectors obtained by numerically diagonalizing the dynamical matrix Eq. (23) (blue). Dots: the results of the numerical minimization as discussed in Sect. 4, for the same parameters $a_{\rm pot} = 5.2\,\mu{\rm m}$, based on a N = 147991 sample.

and frequencies obtained by diagonalizing the dynamical matrix:

$$D(\mathbf{q}) = \frac{K}{m} \begin{pmatrix} 3 - \cos\left(\frac{q_x a_{\text{coll}}}{2}\right) \sin\left(\frac{\sqrt{3}q_y a_{\text{coll}}}{2}\right) - 2\cos\left(\frac{q_x a_{\text{coll}}}{2}\right) & \sqrt{3}\sin\left(\frac{q_x a_{\text{coll}}}{2}\right) \sin\left(\frac{\sqrt{3}q_y a_{\text{coll}}}{2}\right) \\ \sqrt{3}\sin\left(\frac{q_x a_{\text{coll}}}{2}\right) \sin\left(\frac{\sqrt{3}q_y a_{\text{coll}}}{2}\right) & 3 - 3\cos\left(\frac{q_x a_{\text{coll}}}{2}\right) \cos\left(\frac{\sqrt{3}q_y a_{\text{coll}}}{2}\right) \end{pmatrix}.$$

$$(23)$$

Indeed Figure 16 shows that this improvement removes the discontinuity at $\theta=2.2^{\circ}$ and results in a qualitatively similar, but significantly different curve. Moreover, the quantitative agreement with the numerical results improves dramatically as the exact phonon frequencies and eigenvalues are adopted. The analytic weak-coupling curves reported in Fig. 10, 11 are all obtained using this improved evaluation code.

References

- [1] L. M. Floría and J. J. Mazo. Dissipative dynamics of the Frenkel-Kontorova model. *Adv. in Phys.*, 45(6):505–598, 1996.
- [2] A. D. Novaco and J. P. McTague. Orientational epitaxy—the orientational ordering of incommensurate structures. *Phys. Rev. Lett.*, 38:1286–1289, 1977.
- [3] J. P. McTague and A. D. Novaco. Substrate-induced strain and orientational ordering in adsorbed monolayers. *Phys. Rev. B*, 19:5299–5306, 1979.
- [4] S. Pagano, Angular energetics and friction of a harmonic hexagonal monolayer over a quasicrystalline substrate, Diploma thesis (University Milan, 2022), http://materia.fisica.unimi.it/manini/theses/paganoMag.pdf.
- [5] A. Raiteri, Novaco-angle investigation of friction in a colloidal monolayer on a quasicrystalline substrate, Diploma thesis (University Milan, 2019), http://materia.fisica.unimi.it/manini/theses/raiteri.pdf.
- [6] D. Pizzamiglio, A model colloidal monolayer on a quasicrystalline substrate: statics and frictional dynamics, Diploma thesis (University Milan, 2020), http://materia.fisica.unimi.it/manini/theses/pizzamiglio.pdf.
- [7] M. Bellagente, *Sliding on a quasicrystal: a colloidal model*, Diploma thesis (University Milan, 2016), http://materia.fisica.unimi.it/manini/theses/bellagente.pdf.
- [8] Andrea Vanossi, Nicola Manini, and Erio Tosatti. Static and dynamic friction in sliding colloidal monolayers. *Proc. Nat. Acad. Sci. USA*, 109(41):16429–16433, 2012.
- [9] M. Jules, M. Schmiedeberg, S. Rausch, J. Roth, H. Stark, and C. Bechinger. Proliferation of anomalous symmetries in colloidal monolayers subjected to quasiperiodic light fields. *Proc. Nat. Acad. Sci. USA*, 107:7214-8, 2010.
- [10] T. Bohlein J. Mikhael and C. Bechinger. Observation of kinks and antikinks in colloidal monolayers driven across ordered surfaces. *Nat. Mater.*, 11(2):126–130, 2011.

- [11] A. P. Thompson, H. M. Aktulga, R. Berger, D. S. Bolintineanu, W. M. Brown, P. S. Crozier, P. J. in 't Veld, A. Kohlmeyer, S. G. Moore, T. D. Nguyen, R. Shan, M. J. Stevens, J. Tranchida, C. Trott, and S. J. Plimpton. LAMMPS a flexible simulation tool for particle-based materials modeling at the atomic, meso, and continuum scales. Comp. Phys. Comm., 271:108171, 2022.
- [12] W. H. Press, S. A. Teukolsky, W. T. Vetterling, and B. P. Flannery. Numerical recipes in C: the art of scientific computing. Cambridge Univ. Press, Cambridge, 2. ed edition, 1992.
- [13] E. Polak. Computational methods in optimization: a unified approach.

 Mathematics in science and engineering. Academic Press, 1971.
- [14] D. Sheppard, R. Terrell, and G. Henkelman. Optimization methods for finding minimum energy paths. *J. Chem. Phys.*, 128:134106, 2008.
- [15] E. Bitzek, P. Koskinen, F. Gahler, M. Moseler, and P. Gumbsch. Structural relaxation made simple. *Phys. Rev. Lett.*, 97:170201, 2006.
- [16] J. Guénolé, W. G. Nöhring, A. Vaid, F. Houllé, Z. Xie, A. Prakash, and E. Bitzek. Assessment and optimization of the fast inertial relaxation engine (fire) for energy minimization in atomistic simulations and its implementation in LAMMPS. Comp. Mat. Sci., 175:109584, 2020.
- [17] LAMMPS documentation for the harmonic bond. https://docs.lammps.org/bond_harmonic.html.